UC Irvine
UC Irvine Previously Published Works

Title
Synergy between fast-ion transport by core MHD and test blanket module fields in DIII-D experiments

Permalink
https://escholarship.org/uc/item/9w2431rd

Journal
Nuclear Fusion, 55(8)

ISSN
0029-5515

Authors
Heidbrink, WW
Austin, ME
Collins, CS
et al.

Publication Date
2015-08-01

DOI
10.1088/0029-5515/55/8/083023

Copyright Information
This work is made available under the terms of a Creative Commons Attribution License, availalbe at https://creativecommons.org/licenses/by/4.0/

Peer reviewed

eScholarship.org Powered by the California Digital Library
University of California

IOP Publishing | International Atomic Energy Agency Nuclear Fusion

Nucl. Fusion **55** (2015) 083023 (12pp) doi:10.1088/0029-5515/55/8/083023

Synergy between fast-ion transport by core MHD and test blanket module fields in DIII-D experiments

W.W. Heidbrink[1], M.E. Austin[1], C.S. Collins[2], T. Gray[3], B.A. Grierson[4], G.J. Kramer[4], M. Lanctot[5], D.C. Pace[5], M.A. Van Zeeland[5] and A.G. Mclean[6]

[1] University of California Irvine, Irvine, CA 92697, USA
[2] University of Texas at Austin, Austin, TX 78712, USA
[3] Oak Ridge National Laboratory, Oak Ridge, TN, USA
[4] Princeton Plasma Physics Laboratory, Princeton, NJ, USA
[5] General Atomics, San Diego, CA, USA
[6] Lawrence Livermore National Laboratory, Livermore, CA, USA

E-mail: Bill.Heidbrink@uci.edu

Received 27 April 2015, revised 12 June 2015
Accepted for publication 16 June 2015
Published 21 July 2015

Abstract

Fast-ion transport caused by the combination of MHD and a mock-up test-blanket module (TBM) coil is measured in the DIII-D tokamak. The primary diagnostic is an infrared camera that measures the heat flux on the tiles surrounding the coil. The combined effects of the TBM and four other potential sources of transport are studied: neoclassical tearing modes, Alfén eigenmodes, sawteeth, and applied resonant magnetic perturbation fields for the control of edge localized modes. A definitive synergistic effect is observed at sawtooth crashes where, in the presence of the TBM, the localized heat flux at a burst increases from 0.36 ± 0.27 to 2.6 ± 0.5 MW m^{-2}.

Keywords: fast ions, sawtooth, Alfven eigenmodes, neoclassical tearing modes

(Some figures may appear in colour only in the online journal)

1. Introduction

The proposed ITER tritium-breeding test blanket modules (TBMs) [1] are expected to contain ferromagnetic materials that will perturb the nearby plasma with ∼1% local magnetic field reductions. These field perturbations could cause concentrated losses of alpha particles that damage the wall near the TBMs. Calculations [2] indicate that, in the absence of additional fast-ion transport mechanisms, the alpha loss power fraction will be very low, ∼0.2%. The calculated losses are tiny because the perturbing fields are most effective at the plasma edge, where the production of alpha particles is small. However, the concern remains that instabilities may transport alpha particles from the populated core region to the plasma edge, where the TBM fields are effective [2, 3] (figure 1). The combined effect of MHD modes and of TBM fields could be much more dangerous than either in isolation because the TBM fields may concentrate nearly axisymmetric losses from MHD into localized 'hot spots'. The present experiment investigates this possibility.

The experiment uses the mock-up TBM field coils that were previously installed on DIII-D [4]. Although three TBM modules are planned for ITER, the DIII-D mock-up coils are installed at a single toroidal location. To mimic the ITER fields, the DIII-D installation contains two racetrack coils and a vertical solenoid that are both energized in the present experiment. The amplitude of the perturbed field exceeds the amplitude of a single ITER TBM by a factor of ∼3.

Previous experiments found that the mock-up TBM fields degrade both fusion product [4] and beam-ion [5] confinement. During beam injection, localized heating on the graphite tiles that surround the TBM port is observed [5]. Initially, it was unclear whether this additional heating is caused by beam-ion impact or by increased heat flux from the bulk plasma but, in a

 © 2015 IAEA, Vienna Printed in the UK

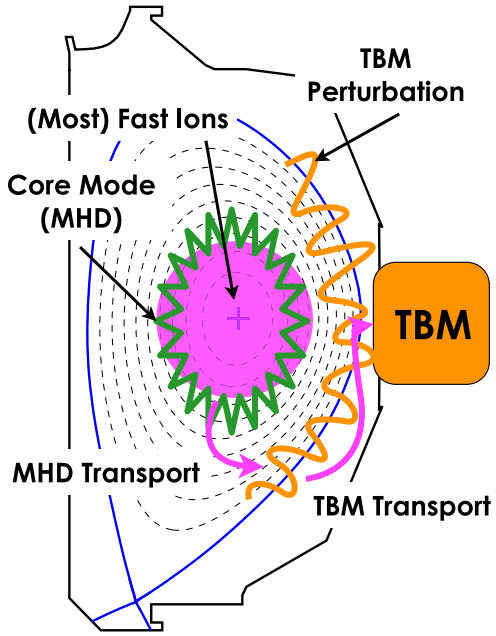

Figure 1. Concept of the experiment. Transport of fast ions by core MHD can populate the edge region, where TBM fields cause concentrated losses.

follow-up experiment [6], 2 MW of beam power was replaced by 3.3 MW of electron cyclotron heating power in plasmas with the same plasma shape. Localized heating was only observed during neutral beam injection, definitively establishing that beam-ion losses are responsible.

The strategy in the present experiment is straightforward: with the TBM either on or off, compare the localized heat flux in plasmas with identical MHD. In some cases, these comparisons are performed in sequential discharges while, in others, comparisons are possible at different times in the same discharge (figure 2). Ideally, to establish synergistic transport between the MHD and the TBM fields, MHD-quiescent discharges with the TBM either on or off would also be obtained but this was generally not possible without altering the plasma conditions.

This paper is organized as follows. After an overview of the DIII-D apparatus (section 2), the synergy data between TBM fields and four different perturbing fields are presented. Section 3 is about synergy with transport by neoclassical tearing modes (NTM), section 4 is about Alfén eigenmode (AE) induced transport, section 5 is about transport by sawteeth, and section 6 is about transport in the presence of combined TBM and resonant magnetic perturbation (RMP) fields. Since a major goal of the present study is to provide data for code benchmarking within the framework of the International Tokamak Physics Activity (ITPA) Topical Group on Energetic Particles, each section contains information on the MHD modes, core fast-ion transport, and localized heating. Section 7 summarizes the results.

2. Apparatus

All plasmas are deuterium discharges heated by deuterium neutral beams with injection energies of 74–81 keV. For these experiments, all of the beamlines are centered on the midplane. The near-perpendicular and near-tangential DIII-D sources have tangency radii of 0.76 m and 1.15 m, respectively. Carbon from the graphite walls is the dominant impurity. The toroidal field is 2.0–2.1 T.

The mock-up TBM coils are unchanged from the previous experiments [4, 5, 7], except that the apparatus was installed at a toroidal angle of 285° rather than at 270° (figure 3). Two sets of coils, the racetrack coil and the solenoid coil, mimic the toroidal and poloidal magnetization of a pair of ITER TBMs in one equatorial port. A current magnitude of 1 kA in both coils produces a spatially localized magnetic field perturbation that is largest on the low field side midplane. (The programmed currents were identical in both coils for all shots in this experiment.) Near the plasma surface ($R = 2.29$ m), the peak radial, vertical, and toroidal magnetic field perturbations are 0.0409, 0.0340, and 0.0129 T, respectively. The calculated [8] outward deflection of the vacuum magnetic field lines near the TBM is $\lesssim$2 mm, a value that is an order of magnitude smaller than the gap between the last-closed flux surface and the vessel wall. Localized heating is caused primarily by orbital deflections across field lines, not free-streaming along deflected field lines [6].

The primary diagnostic of fast-ion loss is an infrared (IR) camera that views the tiles surrounding the TBM coils (figure 3). The measured radiation is related to the tile temperature through calibration of the camera, lens and mirrors with a blackbody source. The heat flux is deduced from the surface temperature by a 1D, semi-infinite model of heat conduction into the tile bulk [9], assuming a heat transmission coefficient for the loosely adhered surface of $\alpha = 10^4$ W m^{-2} K^{-1}. When the TBM coils are energized, the temperature and inferred heat flux generally rise (figure 4). In this study, unless otherwise stated, the quoted heat flux is an average over the 2–3 pixels that are most sensitive to the TBM fields. The location of these pixels changes slightly with plasma conditions but, in all cases, corresponds to the upper right 'hot spot' in figure 4. Because the area of this 'hot spot' is <0.04 m^2, the total lost power is a small fraction of the injected beam power for all of the discharges in this study. For example, for discharge #157 402 (table 1), when the peak heat flux is ~8 MW m^{-2}, the total lost power to the TBM tiles is ~0.2 MW.

DIII-D is also equipped with a pair of scintillator-based fast-ion loss detectors (FILD) [10]. Light from the scintillator is split between a CCD camera that provides pitch and energy resolution and photomultipliers that provide excellent temporal resolution. The data in this paper are photomultiplier signals from the lower FILD detector (figure 3); the signals are from a full-energy spot on the scintillator that observes prompt losses from the counter-injected beams.

Fast-ion D-alpha (FIDA) measurements are the primary diagnostic for the profile of confined fast ions. Most of the data presented here is from the system [11] with an oblique view (figure 3) that is primarily sensitive to co-passing ions. The spectra are integrated between 650.5–652.7 nm; this wavelength range corresponds to energies along the line-of-sight of 25–68 keV. The intensity calibration is obtained from an MHD-quiescent shot. The measurements are compared with the classical signals

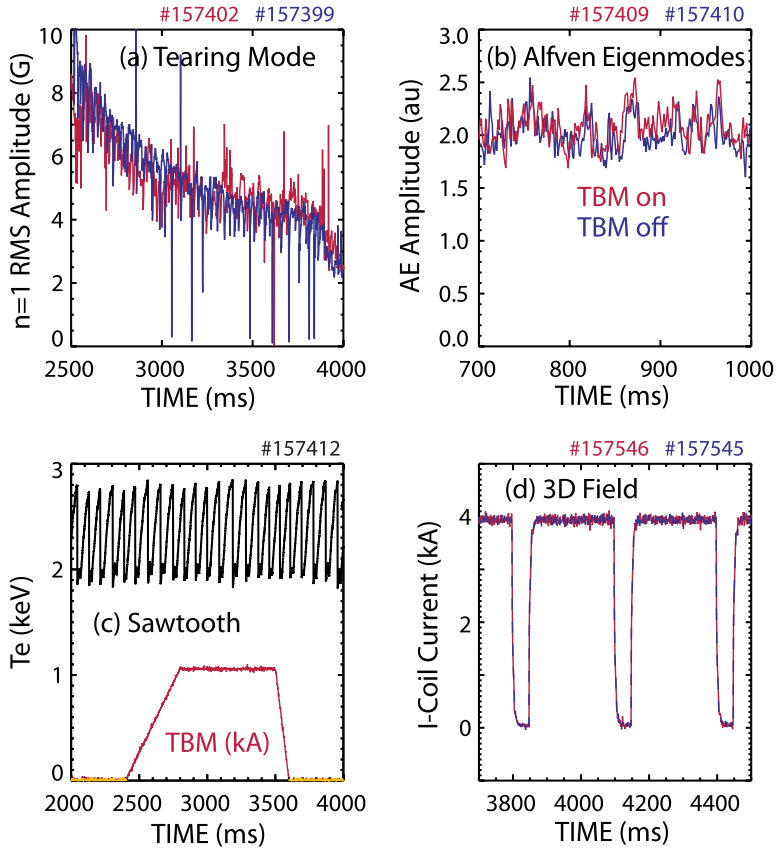

Figure 2. Overview of the experimental strategy. In each portion of the experiment, a different type of MHD (*a*)–(*c*) or applied field (*d*) causes transport. Either successive discharges with or without TBM fields are compared (*a*), (*b*), (*d*) or, in the case of sawteeth (*c*), the time period before and after the TBM pulse is compared with the period with TBM fields.

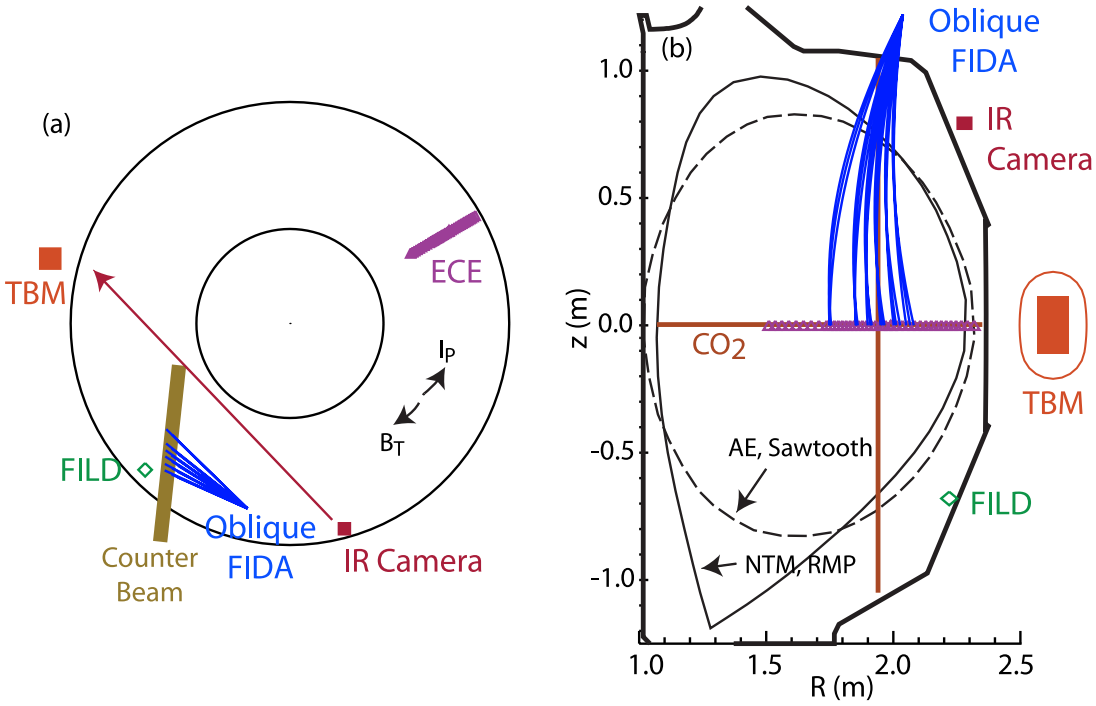

Figure 3. (*a*) Plan view and (*b*) elevation of the DIII-D tokamak, showing the locations of the TBM coils, the IR camera, one of the FILD detectors, the 40-channel ECE array, and the sightlines of the oblique FIDA diagnostic. The plasma shapes for the four experiments are also shown.

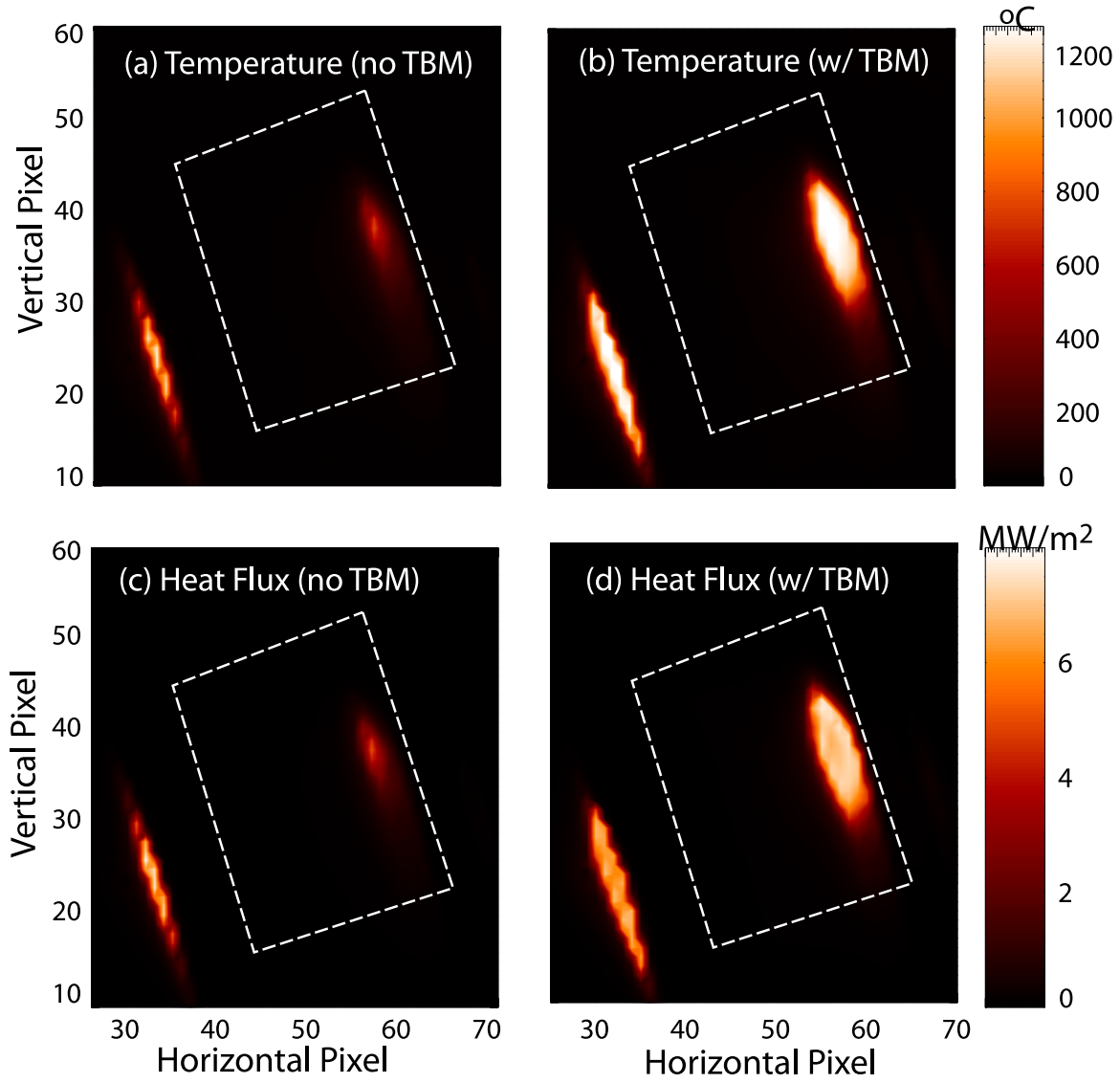

Figure 4. IR camera data for (*a*), (*b*) temperature and (*c*), (*d*) inferred heat flux without (*a*), (*c*) and with (*b*), (*d*) TBM fields in the sawtooth experiment at times 2200 and 2700 ms. Each pixel measures an area of approximately 2×2 cm^2. The dashed line shows the approximate outline of two of the graphite tiles that protect the mock-up TBM coils (see figure 2(*b*)) of [6]).

Table 1. Time-averaged heat flux on the TBM protective tiles (in MW m^{-2}) for the four discharges shown in figure 9.

Shot	2200–2400 ms	2500–2650 ms
157 401	0.42 (no NTM)	0.60 (no NTM)
157 399	1.98	2.66
157 400	4.48	6.93
157 402	1.56	7.74 (TBM)

Note: Discharge #157 401 (first row) did not have an NTM. The only entry with TBM fields is in the lower right corner.

predicted by the synthetic diagnostic code FIDASIM [12] using the distribution function computed by NUBEAM [13]. The error bars are obtained by forming an ensemble of the ratio of measured brightness to predicted brightness at a series of time points, so both measurement errors and errors associated with plasma-profile uncertainties are included.

Typical plasma parameters for the four parts of the experiment appear in figure 5. The electron density (figure 5(*a*)) is measured by Thomson scattering [14] and CO_2 interferometers [15]. The electron temperature (figure 5(*b*)) is measured by Thomson scattering and an electron cyclotron emission (ECE) radiometer [16]. The ion temperature, rotation frequency, and $Z_{\rm eff}$ profiles (figures 5(*c*)–(*e*)) are inferred from charge exchange recombination spectroscopy measurements of carbon [17]. The safety factor profile (figure 5(*f*)) is from EFIT equilibrium reconstructions [18] that use magnetics and motional Stark effect [19] data.

The toroidal (n) and poloidal (m) mode numbers of the instabilities are measured by toroidal and poloidal arrays of magnetic probes [20], while radial profiles are from ECE electron temperature fluctuation measurements.

3. Synergy with neoclassical tearing modes

The plasma shape for the NTM experiments is an elongated ($\kappa \simeq 1.8$), high triangularity ($\delta \simeq 0.6$), divertor configuration

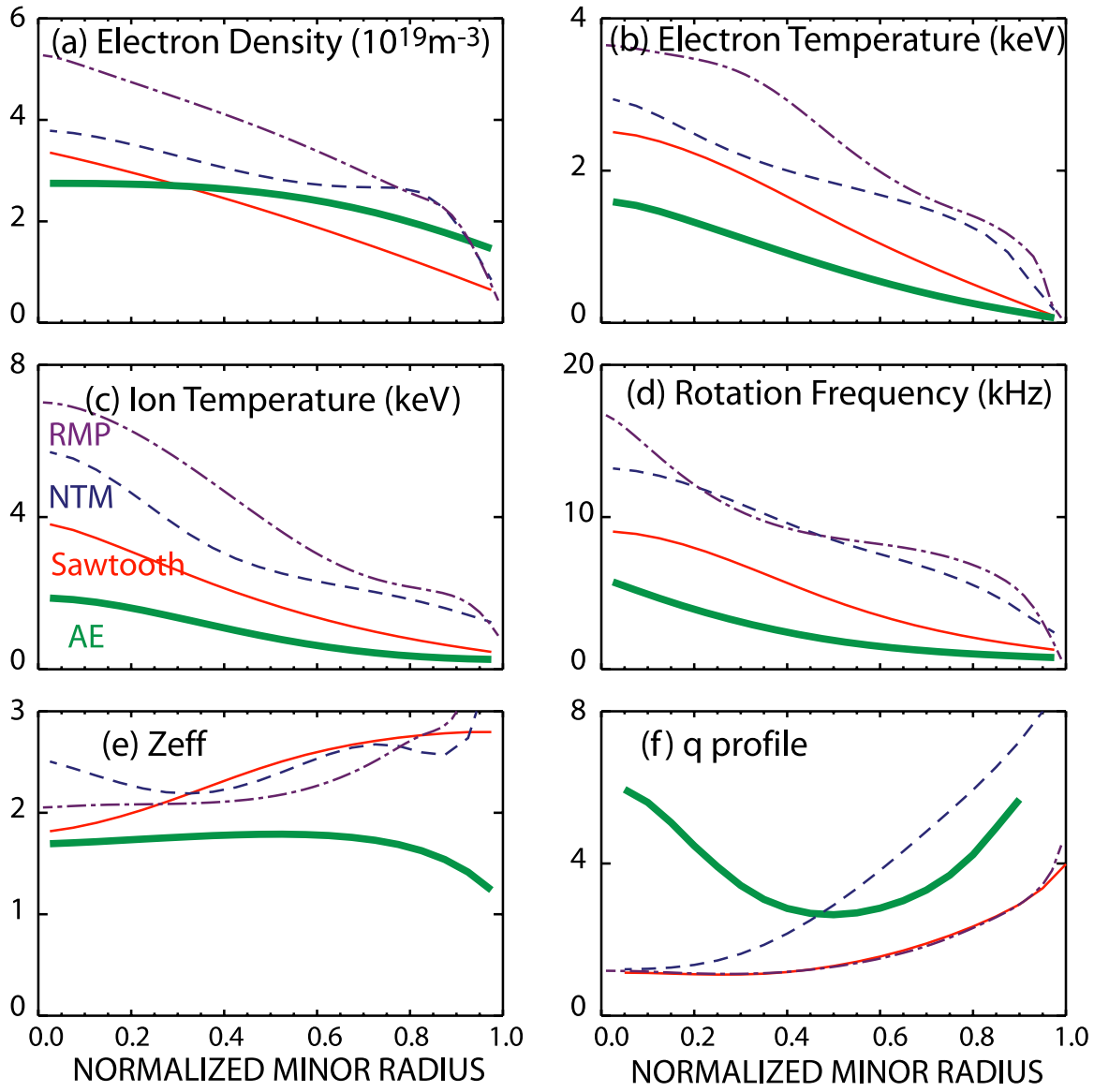

Figure 5. Time-averaged profiles of (*a*) n_e, (*b*) T_e, (*c*) T_i, (*d*) toroidal rotation frequency, (*e*) $Z_{\rm eff}$, and q versus ρ for the NTM (dashed line), AE (thick line), sawtooth (thin line) and RMP (dash-dot line) experiments. The abscissa is the normalized square root of the toroidal flux ρ.

(figure 3(*b*)). The 'outer gap' between the last-closed flux surface and the wall is a relatively large 9.6 cm in these plasmas. The plasma is an H-mode plasma with edge localized modes (ELM). As in previous experiments [21], a series of beam power steps is used to trigger an $m = 2$, $n = 1$ (2/1) tearing mode at ~1900 ms (figure 6). This creates a relatively stationary plasma with a large NTM that has a fairly steady frequency of ~10 kHz between ~2500–3800 ms. During this stationary phase, an average beam power of 5.2 MW is injected, with 9% in the counter near-tangential direction, 32% in the co-near-perpendicular direction, and 59% in the co-near-tangential direction. The TBM coils are energized on some shots but not on others; the mode amplitude is unaffected by the TBM. On some shots, the power burst fails to trigger an NTM.

Figure 7 shows the radial profile of the NTM from ECE. The data show the expected features of an NTM but with some complications. As expected for a resistive 2/1 mode, the T_e profile is flat near the $q = 2$ surface (figure 7(*c*)) and the phase of the oscillation jumps 180° across the $q = 2$ surface (figure 7(*b*)). A complication is that additional poloidal harmonics besides $m = 2$ are present; also, there is a large amplitude oscillation by the outer edge.

If the NTM causes enhanced fast-ion transport, the effect is modest. Figure 8 shows FIDA profiles for three discharges in this series. The discharge without an NTM has the largest signal on the innermost FIDA channel but the difference is within the uncertainty. Similarly, compared to the classical prediction, the neutron rate is higher on the discharge without an NTM but the rate is only 2% and 9% higher than in the two discharges with NTMs.

Application of the TBM fields to these discharges causes an increase in heat flux to the tiles surrounding the coils (figure 9, table 1). Even without TBM fields, the heat flux is enhanced by an NTM. For the two discharges with NTMs but no TBM, the heat flux signals differ considerably despite the fact that

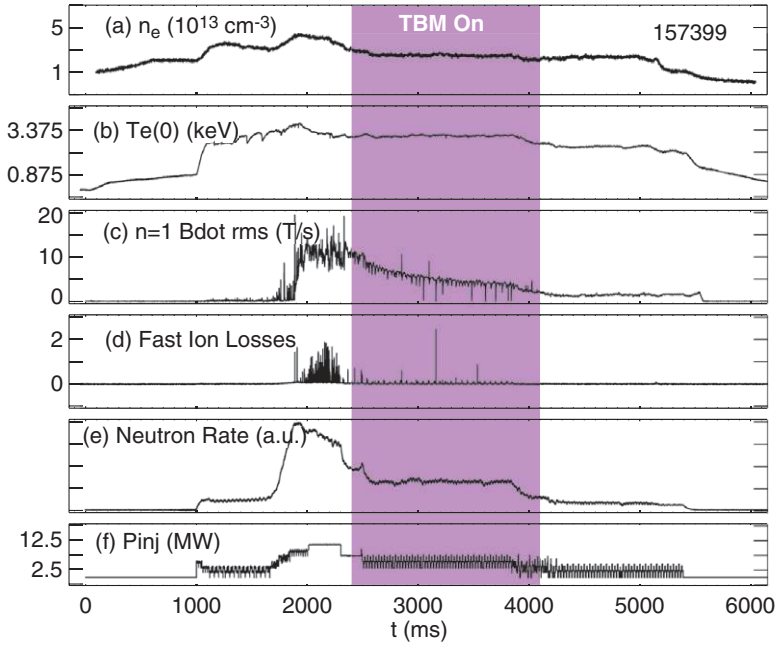

Figure 6. (*a*) Line-averaged density, (*b*) central electron temperature, (*c*) $n = 1$ magnetics signal, (*d*) FILD photomultiplier signal, (*e*) neutron rate, and (*f*) injected beam power for a discharge in the NTM experiment. The period when the TBM field is applied on some of the discharges is indicated. TBM current $I_{TBM} = 0.91$ kA.

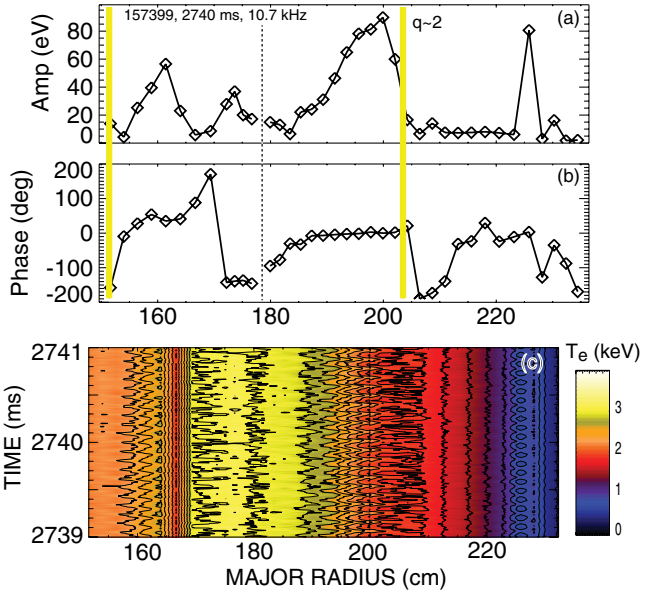

Figure 7. ECE measurements of the radial mode structure of the NTM. (*a*) Amplitude and (*b*) phase from the FFT of the 10.7 kHz NTM. The position of the $q = 2$ surface inferred from the equilibrium reconstruction is indicated by the solid vertical lines; the dotted line represents the magnetic axis. (*c*) Contour plot of the ECE data in the time domain. Flat spots in the temperature profile are evident near the $q = 2$ surface both inside and outside of the magnetic axis. Maxima in the amplitude are also clearly seen, e.g. at $R \simeq 160$ cm.

plasma parameters and MHD activity (NTM characteristics, ELMs, Alfén eigenmodes) are similar in the two shots. In the discharge with the TBM, the heat flux increases locally from ~2 MW m^{-2} to ~8 MW m^{-2} when the TBM is energized. This temporal correlation strongly suggests the increase is caused by the TBM fields; indeed, changes are modest at this time in the 'no TBM' reference shots. In one discharge, an NTM was not excited and the TBM coil tripped off in <100 ms. As expected, this discharge has the smallest heat flux. The heat flux is modest even while the TBM is energized, suggesting that TBM fields alone do not cause large heating in this condition.

If the TBM fields concentrate losses near the coils, this is likely to reduce the fast-ion losses elsewhere. This effect is clearly observed by the FILD diagnostic (figure 10). A beam injected in the counter-current direction produces prompt losses that are detected by the FILD. When the TBM coils are energized, the prompt loss signals are 3–4 times smaller than when the TBM coils are off.

4. Synergy with Alfén eigenmodes

The Alfén eigenmode (AE) portion of the study used plasma conditions that are similar to many previous DIII-D experiments. Early beam injection during the current ramp of an L-mode plasma (figure 11) drives many toroidal AEs and reversed-shear AEs unstable [22]. The plasma shape is a slightly-elongated ($\kappa \simeq 1.3$) oval with a relatively small outer gap of 4.5 cm (figure 3(*b*)). An average beam power of 3.8 MW is injected, with 85% in the co-tangential direction and 15% in the counter-tangential direction. The TBM is energized on some shots but not on others. Strong fast-ion losses are detected by the FILD detectors early in the current ramp [23] (figure 11(*d*)). On some discharges, electron cyclotron heating (ECH) is applied near q_{min} in an attempt to alter the amplitude of the RSAEs [24].

As is typical for these conditions, many small-amplitude AEs are observed, both RSAEs that sweep upward in frequency and TAEs with relatively steady frequencies (figure 12). The modes appear throughout the minor radius: some are

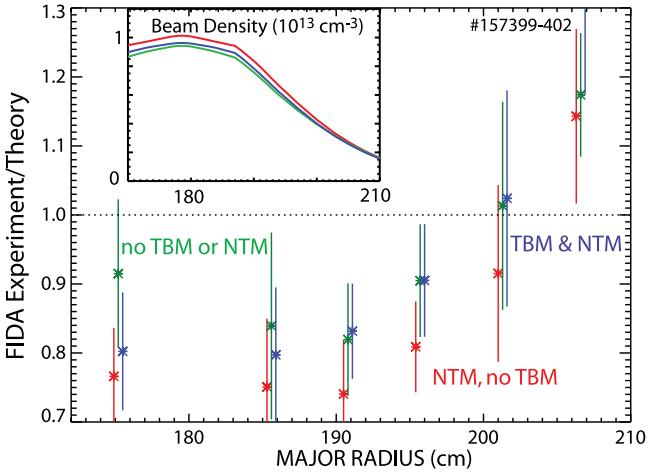

Figure 8. Ratio of FIDA signals to classical FIDASIM predictions versus major radius between 2500–3000 ms for three discharges in the NTM experiment. The inset shows the classical beam density profiles predicted by NUBEAM.

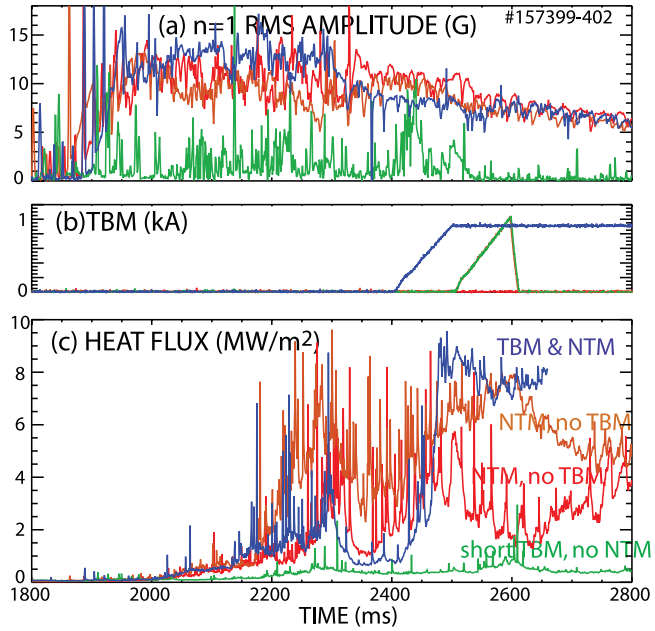

Figure 9. (*a*) NTM mode amplitude, (*b*) TBM current, and (*c*) heat flux versus time for four discharges in the NTM experiment.

co-localized, some are localized near the minimum q radius, and some modes span much of the minor radius. These modes cause strong transport that flattens the fast-ion profile [25]. Figure 13 compares the measured FIDA signal to the expected signal as a function of major radius. In the central quarter of the plasma, the signal is $\lesssim$60% of the classical prediction. Simulations suggest that stochastic diffusive transport by the AEs is responsible for the flattening [26]. Thus, these plasmas are likely to produce synergistic transport between core MHD and edge TBM fields.

Figure 14 compares data from five discharges, two with TBM fields and three without. The amplitude of the AE activity is unaffected by application of the TBM (figure 14(*a*)). The central fast-ion transport, as inferred from the volume-averaged neutron rate, is also insensitive to application of the

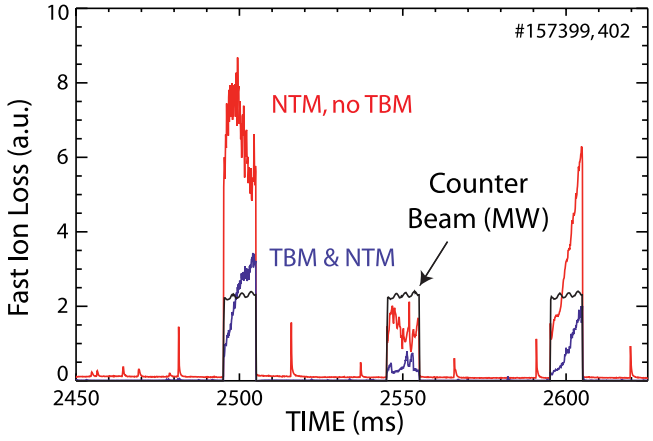

Figure 10. FILD photomultiplier signal during NTM shots with and without TBM fields. The timing of the counter-injected beam is also shown.

TBM (figure 14(*b*)). But the heat flux to the tiles surrounding the TBM coils reproducibly increases by an order of magnitude when the TBM fields are present (figure 14(*d*)).

(In figure 14, the neutron rate steadily approaches the classical prediction despite nearly constant AE mode amplitude. The improving fast-ion confinement is caused by three factors. First, the plasma current steadily increases during this period, so the loss boundaries steadily recede, making AE-induced transport less likely to cause losses. Second, the radius of the minimum q surface moves inward with time, so the majority of mode activity is farther from the plasma edge. Third, the dominant mode activity shifts from TAEs to RSAEs (figure 12). TAEs have broader eigenfunctions than RSAES, so they cause larger fast-ion losses.)

Unfortunately, a similar discharge with TBM fields but without AEs was *not* obtained, so it is impossible to distinguish between transport induced by the TBM coils alone and synergistic transport for this condition. A limited attempt was made to use ECH to alter the virulence of the AE activity but the effect on fast-ion transport was slight (as inferred from the neutron rate) and the heat flux was unaffected.

5. Synergy with sawteeth

The synergy between fast-ion transport by sawteeth and TBM fields was studied in the second half of the AE discharges, during the current flattop (figure 11). The plasma shape remains a slightly-elongated oval with an outer gap of $\sim$4 cm. To maintain the plasma in L-mode, a relatively low average beam power of 4.5 MW is injected, with 10% in the counter near-tangential direction, 52% in the co-near-perpendicular direction, and 38% in the co-near-tangential direction. With an edge safety factor of $q_{95} = 3.4$, the $q = 1$ surface is at a normalized minor radius of $\rho \simeq 0.39$. Very regular sawteeth are observed.

Figure 15 shows details of a representative sawtooth. Both $n = 1$ precursors and $n = 1$ postcursors are observed on the magnetics (figure 15(*a*)). The mode grows explosively in the crash phase. Ninety percent of the drop in central electron temperature occurs in 12 μs (figure 15(*b*)). ECE measurements

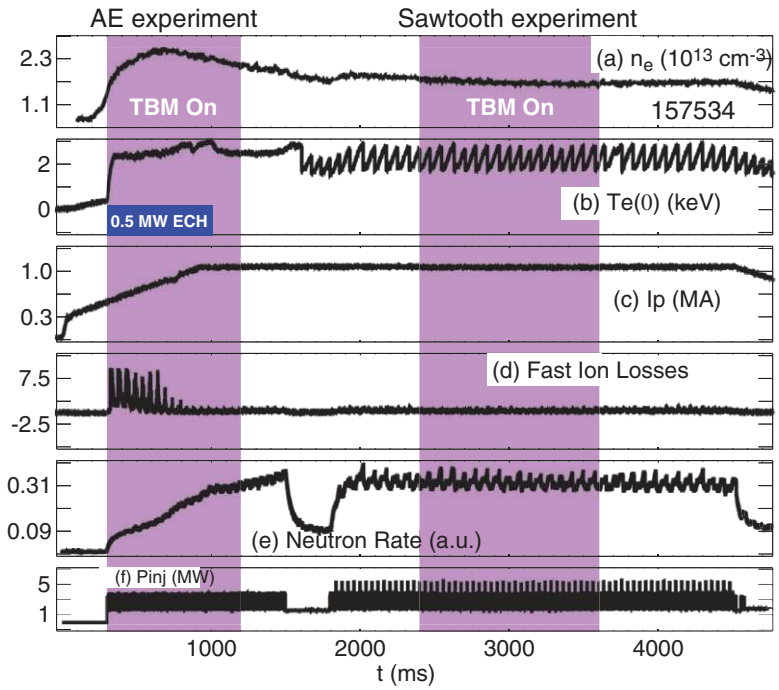

Figure 11. (*a*) Line-averaged density, (*b*) central electron temperature, (*c*) plasma current, (*d*) FILD photomultiplier signal, (*e*) neutron rate, and (*f*) injected beam power for a discharge in the AE and sawtooth experiments. The periods when the TBM field and ECH power are applied on some of the discharges are indicated. TBM current during AE phase: $I_{\mathrm{TBM}} = 0.86$ kA. TBM current during sawtooth phase: $I_{\mathrm{TBM}} = 1.04$ kA.

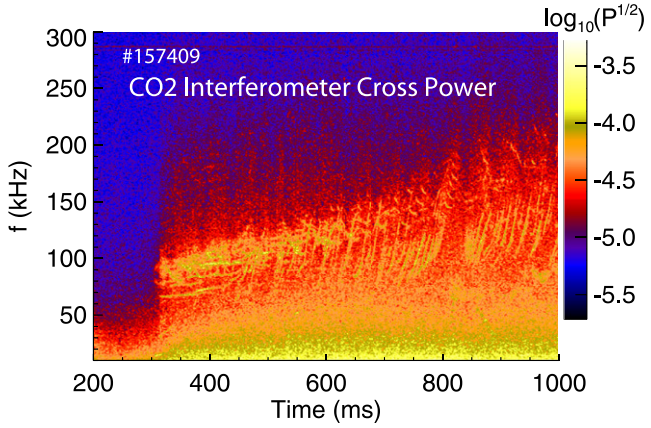

Figure 12. Alfén eigenmode activity measured by the cross-power of two interferometer signals in one of the AE discharges.

show that both the precursor and the postcursor have $m = 1$ structure (figure 15(*d*)). Within the $q = 1$ surface, the measured ECE amplitude of the precursor has approximately a triangle shape (figure 15(*c*)). Taking into account the temperature gradient ∇T_e, the eigenfunction is roughly a 'top-hat' inside $\rho \lesssim 0.2$ but increases in amplitude closer to the $q = 1$ surface.

Information on the amplitude of the displacement is obtained from the ECE data (figure16). The amplitude of the precursor oscillations is ~15 cm peak-to-peak and grows very slowly between 2466–2468 ms. The explosive phase occurs in ~2 cycles, with a final peak-to-peak excursion of ~30 cm.

As in a previous study of fast-ion transport by sawteeth in DIII-D [27], the sawtooth crash transports fast ions from inside the $q = 1$ surface to outside $q = 1$. Figure 17 shows FIDA profiles before and after the sawtooth crash. In general, the FIDA signal depends upon the product of the injected neutral density n_{inj} and the fast-ion density n_f. Since the sawtooth flattens the electron density profile (thereby altering n_{inj}), in principle, changes in FIDA brightness could be caused by changes in neutral density; however, calculations of n_{inj} using n_e before and after the sawtooth crash show that this effect is negligible here. The changes in FIDA brightness in figure 17 reflect changes in fast-ion density n_f. Near the magnetic axis, the signal drops 25–30% while, outside $q = 1$, the signal rises. Previous work on both DIII-D [27] and elsewhere [28, 29] indicate that passing particles usually suffer more transport than trapped particles.

Sawteeth cause increased heat flux to the wall (figure 18). Without TBM fields, the flux jumps up at each sawtooth crash, then gradually relaxes. A possible explanation for the slow recovery is that the sawtooth populates the outer portion of the plasma with fast ions that subsequently collisionally scatter onto loss orbits. (The energy-loss and pitch-angle-scattering times at $\rho = 0.8$ are ~85 and 250 ms, respectively.) Application of TBM fields to these discharges causes a large increase in heat flux to the tiles surrounding the TBM. Increases in the magnitude of the burst at the crash, in the average heat flux, and in the relaxation time following a crash are all observed.

For the four discharges in the experiment, the time-averaged heat flux is 3.5 ± 0.5 times larger with the TBM. In contrast, signals at other toroidal locations, such as FILD detectors or D-alpha light monitors, are unaffected by the TBM.

Figure 19 shows analysis of the bursts in heat flux at each sawtooth crash for the data in figure 18. For these data with

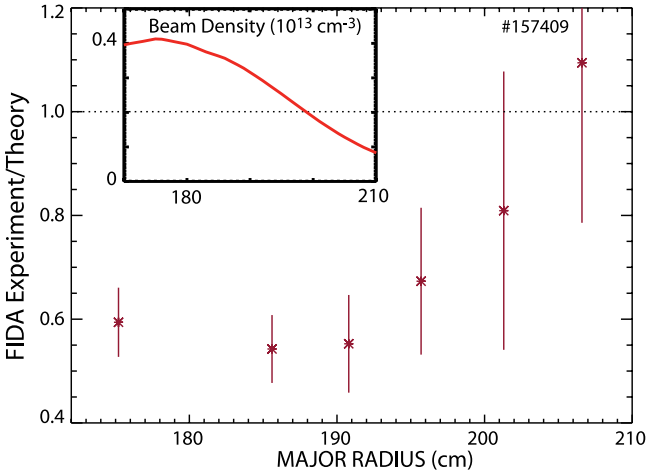

Figure 13. Ratio of FIDA signals to classical FIDASIM predictions between 350–750 ms versus major radius. The inset shows the classical beam density profiles predicted by NUBEAM.

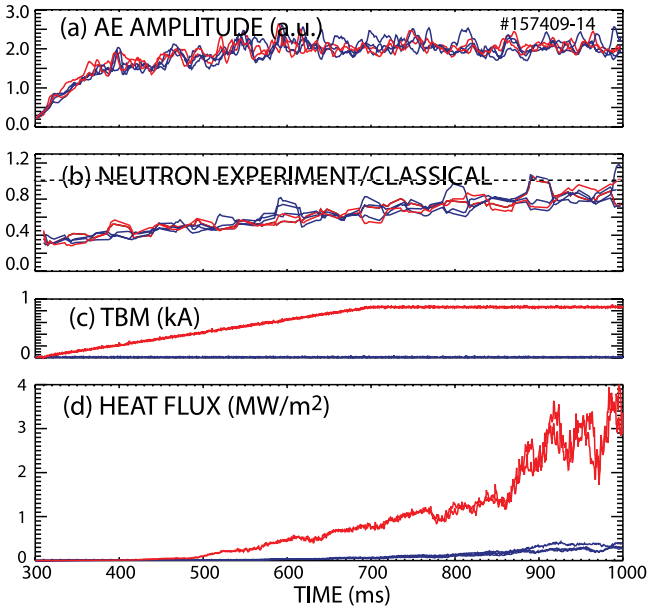

Figure 14. (*a*) AE mode amplitude, (*b*) ratio of measured neutron rate to NUBEAM prediction, (*c*) TBM current, and (*d*) heat flux versus time for five discharges in the AE experiment.

drops in central temperature of 33–42%, the burst in heat flux is uncorrelated with the magnitude of the temperature drop (correlation coefficient $r = -0.02$) but is strongly correlated with the TBM current ($r = 0.91$). The jump in heat flux at a sawtooth is 2.6 ± 0.5 MW m^{-2} when the TBM current exceeds 0.5 kA, compared to 0.36 ± 0.27 MW m^{-2} with the TBM off.

6. Synergy with resonant magnetic perturbation (RMP) fields

The DIII-D tokamak is equipped with a set of six internal coils (I-coils) above and below the midplane that are spaced uniformly in the toroidal direction and designed to make a radial field perturbation of up to 0.0120 T at the coil location

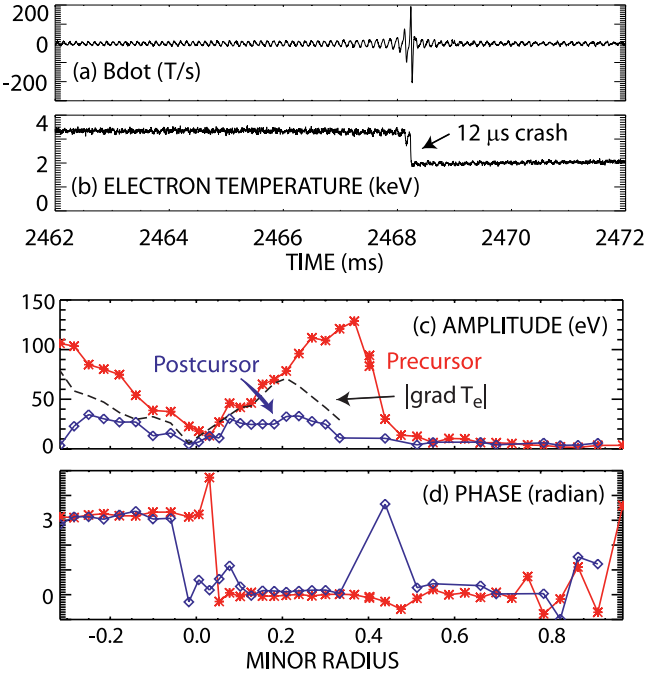

Figure 15. Time evolution of (*a*) a magnetics signal and (*b*) $T_e(0)$ at a sawtooth crash. (*c*) Amplitude and (*d*) phase of the precursor prior to the explosive growth and the postcursor after the crash versus ρ as measured by ECE. The dashed line shows the average value of $|\nabla T_e|$ (a.u.). The frequency of the precursor (postcursor) is 8.8 (8.3) kHz.

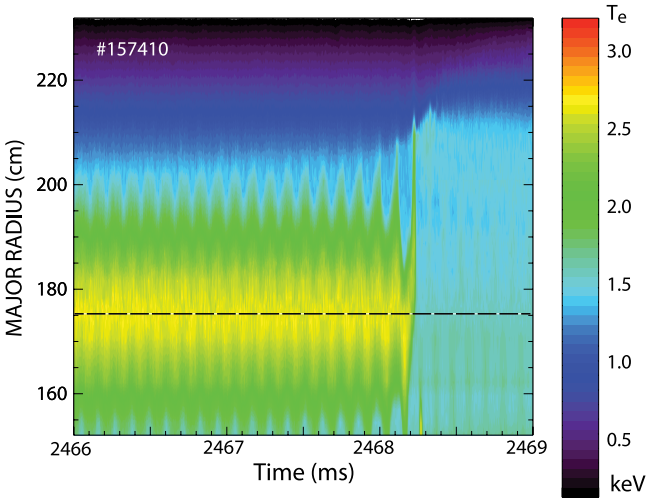

Figure 16. Contours of electron temperature versus time and major radius for the same sawtooth as in figure 15. The dashed line represents the position of the magnetic axis.

immediately behind the first wall. Application of 3D fields with the DIII-D internal coils ('I-coils') can suppress ELMs [30]. In the present experiment, ELMs are suppressed by $n = 3$ odd-parity RMP fields, then TBM fields are added to assess the effect on the concentrated heat flux.

Figure 20 shows a typical discharge. The plasma shape is a high-triangularity divertor, as in the NTM experiment (figure 3(*b*)). The outer gap is 7 cm. Large ELMs occur prior to application of the $n = 3$ field but these are suppressed approximately 300 ms after the field is applied (figure 20(*c*)).

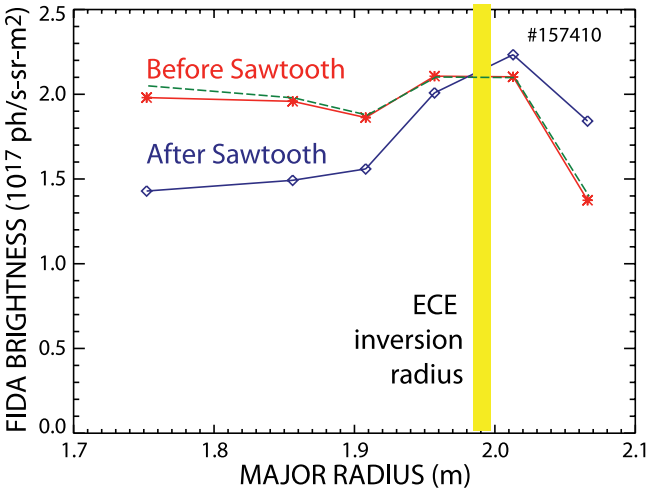

Figure 17. FIDA signal before and after the sawtooth crash shown in figures 15 and 16. The temperature inflection point measured by ECE is indicated by the vertical line. The dashed line represents the expected change in profile caused by changes in the injected neutral density.

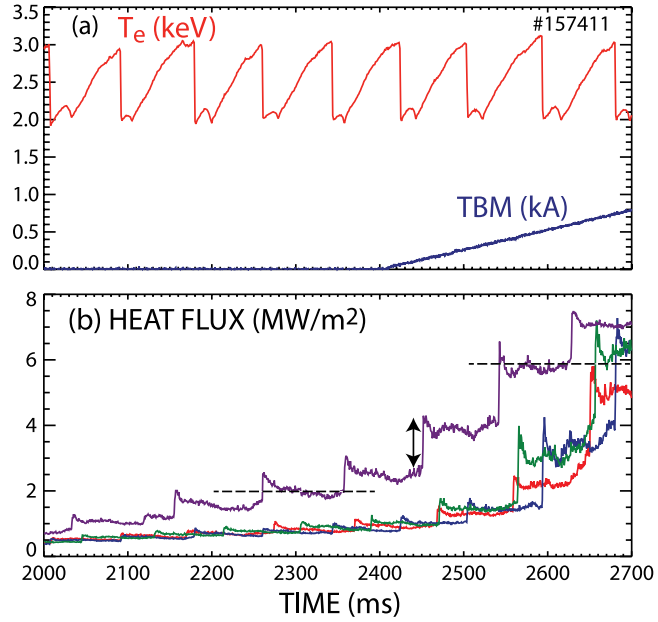

Figure 18. (*a*) Central electron temperature, TBM current, ECCD power, and (*b*) heat flux versus time for four discharges in the sawtooth experiment. The dashed lines show time-averaged values that appear in table 2. The vertical line with arrows shows a heat-flux burst that is plotted in figure 19.

Normally, the $n = 3$ field is continuously applied but, in order to distinguish between TBM and $n = 3$ induced losses, 50 ms 'notches' are applied to the I-coil waveforms (figure 20(*b*)). ELM suppression is sustained during these brief intervals. The density drops when the I-coil current is applied and begins to recover during the notches (figure 20(*a*)). Apart from a ~35% drop in toroidal rotation, application of the TBM fields has little effect on plasma parameters such as the stored energy or neutron rate. During the TBM pulse, an average beam power of 6.3 MW is injected, with

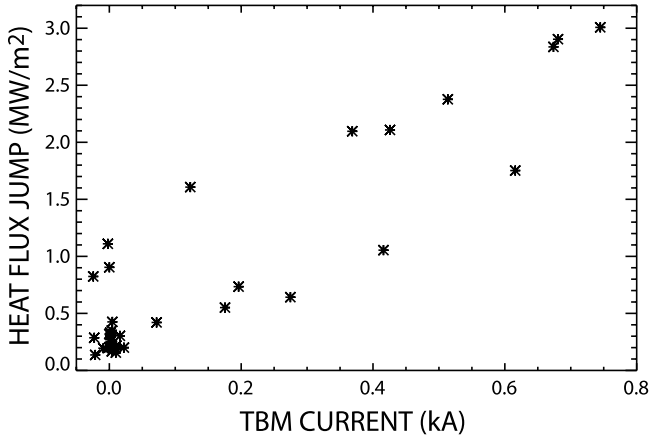

Figure 19. Jump in heat flux at sawtooth crashes versus TBM current.

38% from co-near-perpendicular sources and 62% from co-near-tangential sources.

The effect of the $n = 3$ fields on fast-ion confinement (in the absence of TBM fields) is documented in a recent paper [31]. The $n = 3$ fields cause a ~50% reduction in FIDA channels outside $\rho \gtrsim 0.95$. Full-orbit modeling indicates that passing ions are most affected. Figure 21 shows similar FIDA data when the TBM is energized. With both I-coil and TBM fields, the FIDA signals are lower than without TBM fields but the effect is comparable to the uncertainty in the measurement. (A complication in the interpretation of figure 21 is an MHD event at 3761 ms. This event is correlated with a sudden drop in neutron rate and may be responsible for the low values of the FIDA density at 3805 ms. A similar event did *not* occur on the 'no TBM' reference discharge.)

Application of TBM fields causes a modest ~0.2 MW m^{-2} increase in heat flux to the tiles (figure 22). Although the magnitude of the increase is modest, the fractional increase in the time-average heat flux is appreciable (a factor of 3.3 times larger with TBM). Both with and without the TBM, the flux decreases when the I-coil turns off for 50 ms, demonstrating that the $n = 3$ fields contribute to the localized heating. For the three 'notches' in the I-coil field, the reduction in heat flux is $15 \pm 3\%$ without the TBM and $12 \pm 2\%$ with the TBM.

7. Summary and discussion

Results of the four experiments are summarized in table 2. In all cases, TBM fields increase the time-averaged localized heat flux.

Increased heat flux does not by itself indicate a synergistic effect between MHD-induced transport and TBM-induced transport, as enhancements were previously observed that are not attributed to MHD [5, 6]. Ideally, data would exist in these four quadrants:

1. no MHD, no TBM,
2. w/ MHD, no TBM,
3. no MHD, w/ TBM,
4. w/ MHD, w/ TBM.

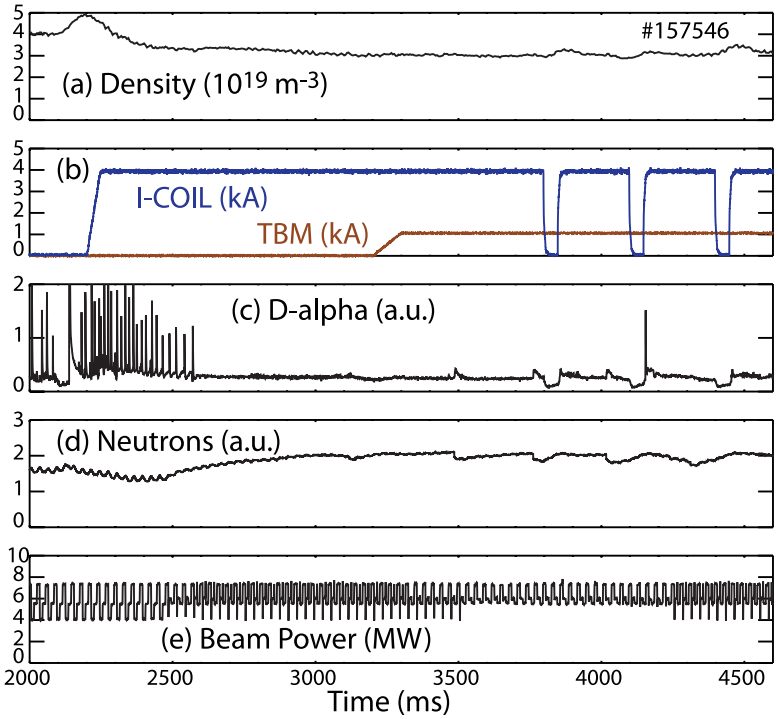

Figure 20. (*a*) Line-averaged density, (*b*) I-coil and TBM currents, (*c*) divertor D-alpha signal, (*d*) neutron rate, and (*e*) injected beam power for a discharge in the RMP experiment. TBM current $I_{TBM} = 1.06$ kA.

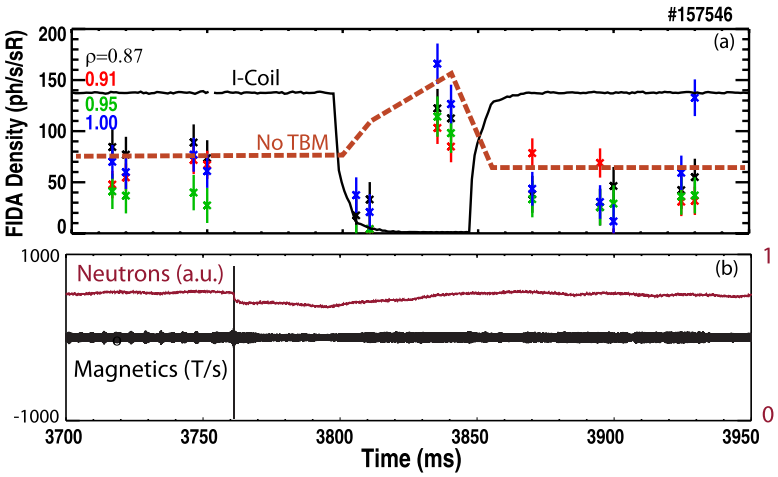

Figure 21. (*a*) FIDA signal divided by injected neutral density versus time for four tangentially viewing channels near the plasma edge. (The normalized minor radius is indicated.) The FIDA spectra are integrated from 659.5–661.5 nm. The I-coil waveform is also indicated. The dashed line represents the FIDA signals at $\rho \simeq 1.0$ in the corresponding 'no-TBM' discharge, #157 545. (*b*) Magnetics and neutron signals. An MHD event at 3761 ms transiently degrades fast-ion confinement.

Complete coverage of this sort was obtained for the sawtooth bursts and for the RMP experiment. Consequently, it can be definitely stated that the combination of fast-ion transport at the sawtooth crash with TBM fields resulted in an increase in concentrated losses (figure 19). In the RMP study, the peak heat flux with both $n = 3$ and TBM fields is $14 \pm 2\%$ larger with combined fields than with TBM fields alone.

The absence of quadrant #3 for the NTM and AE cases prevents a definitive demonstration of synergistic transport for these cases. In light of the large AE-induced transport measured in the core (figure 13), it seems very likely that the TBM heat flux was enhanced by the Alfén eigenmodes but there is no proof that this is the case. For the NTM condition, the concentrated heat flux is relatively large even prior to application of the TBM, suggesting that the NTM plays a role in fast-ion transport. When the TBM is applied, the heat flux rapidly increases (figure 9) and the FILD signal decreases (figure 10), further suggesting synergistic transport. On the other hand, the modest changes in core fast-ion confinement (figure 8) suggest that other factors besides synergistic transport could be operative.

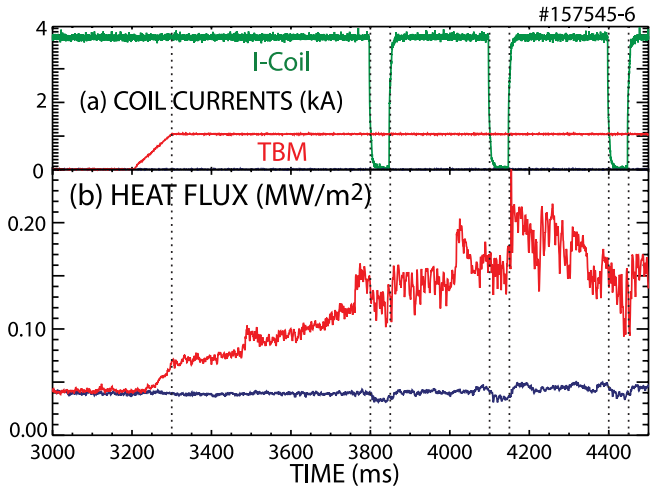

Figure 22. (*a*) I-coil and TBM coil currents and (*b*) heat flux versus time in a pair of discharges with and without TBM fields.

Table 2. IR camera measurements of the time-averaged heat flux on the TBM protective tiles for the four experiments.

Field	w/o TBM (MW m^{-2})	w/ TBM (MW m^{-2})	w/o Time (s)	w/ Time (s)
NTM	1.6-6.9	7.7	2.2–2.4	2.5–2.65
AE	0.2–0.4	2.8–2.9	0.9–1.0	0.9–1.0
Sawtooth	0.8–2.0	2.7–5.8	2.2-2.4	2.5–2.7
RMP	0.04	0.13	3.3–4.5	3.3–4.5

Note: The range in observed values for different discharges of the same type is given. The last two columns list the selected averaging intervals.

The implications of these data for ITER are beyond the scope of this paper. The purpose of this paper is to provide well-documented cases for benchmarking of computer codes. The data for all four cases are posted at the ITPA Energetic Particle website [32] and the DIII-D link listed below. Successful benchmarking against DIII-D experimental data will improve the reliability of ITER predictions. Concentrated losses of alphas at sawteeth in the ITER baseline scenario is a particularly important issue for future research.

Acknowledgments

This work was supported by the U.S. Department of Energy under SC-G903402, DE-AC52-07NA27344, DE-FG03-97ER54415, DE-AC05-0000R22725, DE-AC02-09CH11466, and DE-FC02-04ER54698. We thank R. Nazikian and C. Petty for helpful suggestions, D. Orlov for the TRIP3D calculation, and the entire DIII-D team for their support. DIII-D data shown in this paper can be obtained in digital format by following the links at https://fusion.gat.com/global/D3D_DMP.

References

[1] Ginacarli L. *et al* 2010 *Fusion Eng. Des.* **85** 1829
[2] Shinohara K. *et al* 2011 *Nucl. Fusion* **51** 063028
[3] Snicker A., Hirvijoki E. and Kurki-Suonio T. 2013 *Nucl. Fusion* **53** 093028
[4] Schaffer M.J. *et al* 2011 *Nucl. Fusion* **51** 103028
[5] Kramer G.J. *et al* 2011 *Nucl. Fusion* **51** 103029
[6] Kramer G.J. *et al* 2013 *Nucl. Fusion* **53** 123018
[7] Kramer G.J. *et al* 2013 *Plasma Phys. Control. Fusion* **55** 025013
[8] Evans T.E., Moyer R.A. and Schoch P. M. 2002 *Phys. Plasma* **9** 4957
[9] Carslaw H.S. and Jaeger J. C. 1959 *Conduction of Heat in Solids* (Oxford: Oxford University)
[10] Fisher R.K. *et al* 2010 *Rev. Sci. Instrum.* **81** 10D307
[11] Muscatello C.M., Heidbrink W.W., Taussig D. and Burrell K. H. 2010 *Rev. Sci. Instrum.* **81** 10D316
[12] Heidbrink W.W., Liu D., Luo Y., Ruskov E. and Geiger B. 2011 *Commun. Comput. Phys.* **10** 716
[13] Pankin A., Mccune D., Andre R., Bateman G. and Kritz A. 2004 *Comput. Phys. Commun.* **159** 157
[14] Carlstrom T.N. *et al* 1992 *Rev. Sci. Instrum.* **63** 4901
[15] Carlstrom T.N., Ahlgren D.R. and Crosbie J. 1988 *Rev. Sci. Instrum.* **59** 1063
[16] Austin M.E. and Lohr J. 2003 *Rev. Sci. Instrum.* **74** 1457
[17] Gohil P., Burrell K.H., Groebner R.J. and Seraydarian R. P. 1990 *Rev. Sci. Instrum.* **61** 2949
[18] Lao L.L., St. John H., Stambaugh R.D., Kellman A.G. and Pfeiffer W. 1985 *Nucl. Fusion* **25** 1611
[19] Rice B.W., Nilson D.G. and Wroblewski D. 1995 *Rev. Sci. Instrum.* **66** 373
[20] Strait E. J. 2006 *Rev. Sci. Instrum.* **77** 023502
[21] Petty C.C. *et al* 2004 *Nucl. Fusion* **44** 243
[22] Van Zeeland M.A. *et al* 2006 *Phys. Rev. Lett.* **97** 135001
[23] Pace D.C., Fisher R.K., García-Muñoz M., Heidbrink W.W. and Van Zeeland M. A. 2011 *Plasma Phys. Control. Fusion* **53** 062001
[24] Van Zeeland M.A. *et al* 2008 *Plasma Phys. Control. Fusion* **50** 035009
[25] Heidbrink W.W. *et al* 2007 *Phys. Rev. Lett.* **99** 245002
[26] White R.B., Gorelenkov N., Heidbrink W.W. and Van Zeeland M. A. 2010 *Plasma Phys. Control. Fusion* **52** 045012
[27] Muscatello C.M. *et al* 2012 *Plasma Phys. Control. Fusion* **54** 025006
[28] Nielsen S.K. *et al* 2011 *Nucl. Fusion* **51** 063014
[29] Geiger B. *et al* 2014 *Nucl. Fusion* **54** 022005
[30] Evans T.E. *et al* 2004 *Phys. Rev. Lett.* **92** 235003
[31] Van Zeeland M.A. *et al* 2015 *Nucl. Fusion* **55** 073028
[32] *ITER 2015 ITPA Energetic Particle Physics Topical Group* www.iter.org/org/team/fst/itpa/ep.